PAPER

Three pillared-layered inorganic–organic hybrid polymers with efficient luminescence†

Xi Liu, [ID] * Zhen Zhao, Chun-Hai Wang, Shan Fu and Kun-Lin Huang

Three pillared-layered inorganic–organic hybrid polymers, namely, $[Cu_2(4,4'-Hbpt)(SCN)_2]_n$ (**1**), $[Cd(4,4'-Hbpt)(SCN)_2]_n$ (**2**), and $[Cd(4,4'-Hbpt)(SCN)_2 \cdot CH_3CN]_n$ (**3**) were synthesized *via* layer diffusion methods. In all three complexes, there exist 2-D neutral wave-like d^{10} metal thiocyanate layers (for **1**, $[Cu_2(SCN)_2]_n$, and for **2** and **3**, $[Cd(SCN)_2]_n$) with (4, 4) topology, which are further connected by bidentate 4,4'-Hbpt ligands to form 3-D structures with the primitive cubic topology. The results of photoluminescence and thermogravimetric analyses indicate that the three complexes are good candidates as luminescent materials. This paper provides a strategy to synthesize a novel family of pillared-layered inorganic–organic hybrid polymers constructed with layered d^{10} metal thiocyanate layers and conjugated organic spacers at the molecular engineering level, as well as the discovery of new patterns of crystallization at the crystal engineering level.

Introduction

Inorganic–Organic Hybrid Polymers (IOHPs) constructed from inorganic solids and functional organic ligands have attracted increasing attention from chemists owing to their potential applications in the fields of luminescent devices, electrical conductivity, molecular magnetism, catalysis, molecular absorption, and host–guest chemistry.[1] IOHPs combine the advantageous properties of inorganic, organic, and polymeric materials, and also allow concomitant but separate molecular design of inorganic parts with low dimensions and organic parts as spacers, controllers, and templates at the molecular engineering level. The design of inorganic parts is extremely important because the preferred backbones of inorganic parts may determine the topologies of the coordination framework, especially for structures containing various similar organic ligands. Among various inorganic parts in IOHPs, layered transition metal thiocyanates[2,3] especially d^{10} metal thiocyanates[3] have rarely been introduced to IOHPs. There are three main reasons that drive us to focus on the d^{10} metal thiocyanates as inorganic parts in IOHPs: (1) as a part of our continuing investigations[4] on luminescent d^{10} metal coordination polymers, the incorporation of d^{10} metals in IOHPs is of great

interest in view of their remarkable photophysical and photochemical properties based on their d^{10} electronic configurations,[5] which should lead to interesting new functional luminescent materials. (2) SCN^- is a highly versatile ambidentate ligand with two donor atoms. It may coordinate metal ions through either the nitrogen or the sulfur atom, or both, giving rise to linkage isomers or frameworks of varied dimensionalities.[6] (3) recent studies[3a] on IOHPs containing layered d^{10} metal thiocyanates have shot light on their interesting photoluminescence properties, while how to obtain these complexes with specific topologies and desirable luminescent properties, and sort out the relationship between the structures and physicochemical properties still remain a big challenge.

On the other hand, the appropriate design or selection of organic ligands is undoubtedly another key role in assembling IOHPs with specific topologies and desirable properties. Conjugated organic spacers, for examples, 3,5-bis(*n*-pyridyl)-1,2,4-triazoles are typical dipyridyl ligands with a slightly bent backbone, and attract considerable interest in construction of IOHPs with diverse intriguing networks.[7] Furthermore, conjugated organic ligands are usually possessing good potential ability to enhance photoelectron transfer due to their extended π-electron conjugated systems.[8] Accordingly, the combination of inorganic layers of d^{10} metal thiocyanates and conjugated organic ligands may lead to a novel class of pillared-layered IOHPs with special structural architectures and excellent properties. In this paper, d^{10} metal thiocyanates and 3,5-bis(4-pyridyl)-1,2,4-triazole (4,4'-Hbpt) were selected to assemble three novel pillared-layered IOHPs, namely, $[Cu_2(4,4'-Hbpt)(SCN)_2]_n$ (**1**), $[Cd(4,4'-Hbpt)(SCN)_2]_n$ (**2**), and $[Cd(4,4'-Hbpt)(SCN)_2 \cdot CH_3CN]_n$ (**3**) with neutral wave-like d^{10} metal thiocyanate layers and conjugated organic spacers. In addition,

Chongqing Key Laboratory of Inorganic Functional Materials, College of Chemistry, Chongqing Normal University, Chongqing 401331, P. R. China. E-mail: xliu@cqnu. edu.cn; Fax: +86-023-65362777; Tel: +86-023-65910310

crystal structures, photoluminescent properties, the relationships between the structures and photoluminescence, thermal stabilities of the three complexes were also investigated.

Experimental section

Materials and instrumentation

The ligand 3,5-bis(4-pyridyl)-1,2,4-triazole was prepared according to our previous reported method.[9] Other chemicals were obtained from commercial sources and were used without further purification. The FT-IR spectra were recorded from KBr pellets on a FT-IR 8400S (CE) in the range 4000–400 cm^{-1}. C, H, and N elemental analyses were carried out on a Vario EL III elemental analyzer. X-ray powder diffraction data were recorded with Cu Kα radiation ($\lambda = 1.5406$ Å) on a XRD-6100 with a scan speed of 2° min^{-1}. Thermogravimetric analyses were performed on a HENVEN-HJ HCT-3 thermoanalyzer at a heating rate of 10 °C min^{-1} under an air atmosphere. Photoluminescence analyses were measured on a Perkin-Elmer LS55 fluorescence spectrometer.

Synthesis of [Cu$_2$(4,4′-Hbpt)(SCN)$_2$]$_n$ (1)

Method A

Layer diffusion method. Solution of 4,4′-Hbpt·2H$_2$O (5.2 mg, 0.02 mmol) in ethanol (2 mL) was layered over a solution of CuSCN (4.9 mg, 0.04 mmol) in saturated KSCN water solution (2 mL). Over three days, red crystals were obtained in 55% yield (based on 4,4′-Hbpt). Anal. calc. for C$_{14}$H$_9$Cu$_2$N$_7$S$_2$ (466.48): C, 36.05; H, 1.94; N, 21.02. Found: C, 36.04; H, 1.95; N, 21.02. FT-IR (KBr pellet, ν/cm^{-1}): 2120(s), 1582(w), 1543(w), 1491(w), 1422(s), 1366(m), 1140(m), 1059(m), 1013(w), 835(m), 754(s), 721(m), 532(m), 494(w). ν(C≡N) vibration of SCN$^-$ anions: 2120(s).

Method B

Hydrothermal synthesis method. A mixture of 4,4′-Hbpt·2H$_2$O (5.2 mg, 0.02 mmol), Cu(NO$_3$)$_2$·3H$_2$O (9.6 mg, 0.04 mmol), KSCN (7.8 mg, 0.08 mmol) and CH$_3$CN/H$_2$O (3 mL, v/v = 1 : 2) was sealed in a 25 mL Teflon-lined stainless-steel reactor. The reactor was held at 80 or 120 °C for 3 days, and then was cooling to room temperature at a rate of 10 °C h^{-1}. Red block crystals were obtained in 60% yield (based on 4,4′-Hbpt).

Synthesis of [Cd(4,4′-Hbpt)(SCN)$_2$]$_n$ (2)

An aqueous solution (2 mL) of Cd(NO$_3$)$_2$·4H$_2$O (6.2 mg, 0.02 mmol), KSCN (7.8 mg, 0.08 mmol) in a glass tube was carefully added a buffer layer of CH$_3$CH$_2$OH (1 mL). An ethanol solution (2 mL) of 4,4′-Hbpt·2H$_2$O (5.2 mg, 0.02 mmol) was introduced dropwise to form a third layer. The light-yellow rhombus crystals of **2** were obtained on inter-diffusion of the reactants in three days with 50% yield (based on 4,4′-Hbpt). Anal. calc. for C$_{14}$H$_9$CdN$_7$S$_2$ (451.80): C, 37.22; H, 2.00; N, 21.70. Found: C, 37.23; H, 2.01; N, 21.68. FT-IR (KBr pellet, ν/cm^{-1}): 2104(s), 1587(w), 1547(w), 1491(w), 1422(s), 1368(m), 1142(m), 1063(m), 1011(w), 849(m), 756(m), 727(s), 507(m), 455(w). ν(C≡N) vibration of SCN$^-$ anions: 2104(s).

Synthesis of [Cd(4,4′-Hbpt)(SCN)$_2$·CH$_3$CN]$_n$ (3)

Suitable amount of NH$_4$SCN were added to an aqueous suspension (2 mL) of CdCO$_3$ (5.7 mg, 0.04 mmol), and the mixture were stirred until CdCO$_3$ solid were almost dissolved. The resulting solution was transferred to a glass tube, and then was carefully added a buffer layer of CH$_3$CN (1 mL). A CH$_3$CN solution (1 mL) of 4,4′-Hbpt·2H$_2$O (5.2 mg, 0.02 mmol) was introduced dropwise to form a third layer. The light-brown block crystals of **3** were obtained on inter-diffusion of the reactants in five days with 46% yield (based on 4,4′-Hbpt). Anal. calc. for C$_{16}$H$_{12}$CdN$_8$S$_2$ (492.86): C, 38.99; H, 2.45; N, 22.74. Found: C, 38.43; H, 2.33; N, 21.57. FT-IR (KBr pellet, ν/cm^{-1}): 3443(b,s), 2104(s), 2075(s), 1994(m), 1618(m), 1587(m), 1547(m), 1524(w), 1495(w), 1466(w), 1423(s), 1369(m), 1315(w), 1219(w), 1140(w), 1061(w), 1013(w), 840(w), 758(m), 729(s), 507(w), 453(w). ν(C≡N) vibration of SCN$^-$ and CH$_3$CN anions: 2104(s), 2075(s).

X-ray single crystal structure determinations

Suitable single crystals of **1**, **2** and **3** were carefully selected under an optical microscope and glued to thin glass fibers. Data collections were performed on a Rigaku Mercury CCD diffractometer equipped with a graphite monochromated Mo Kα radiation ($\lambda = 0.71073$ Å) at 293 K. The intensity data sets were collected with an ω-scan technique and reduced by Crystal Clear 1.35 software.[10] The structures were solved by direct methods and refined by full-matrix least squares techniques. Non-hydrogen atoms were located by difference Fourier maps and subjected to anisotropic refinement. Hydrogen atoms were added according to the theoretical models. All of the calculations were performed by the Siemens SHELXTL version 5 package of crystallographic software.[11] Crystallographic data and structural refinements for **1**, **2** and **3** are summarized in Table 1. Selected bond lengths and angles were summarized in Table 2. More details on the crystallographic studies as well as atom displacement parameters are given as ESI.†

Results and discussion

Synthesis and general characterization

As described above, complex **1** could be obtained by two methods, namely, layer diffusion method and hydrothermal synthesis method. However, the red crystals obtained *via* hydrothermal synthesis could not be determined by X-ray single crystal analysis due to their poor crystallinity, which were confirmed to be the same as those were synthesized *via* layer diffusion method, by elemental analyses, IR spectroscopy, and PXRD. For the synthesis of **2**, the buffer layer of CH$_3$CH$_2$OH solvent is important since it could effectively prevent the emergence of precipitates. And for the synthesis of **3**, the amount of NH$_4$SCN mainly depends on the solubility of the CdCO$_3$ and complexation constant of Cd(SCN)$_4$$^{2-}$ in aqueous solution at room temperature, the mixture of NH$_4$SCN and CdCO$_3$ in aqueous solution should be filtered before transferred to a glass tube.

Table 1 Crystal and structure refinement data for **1**, **2** and **3**[a]

Complexes	1	2	3
Formula	$C_{14}H_9Cu_2N_7S_2$	$C_{14}H_9CdN_7S_2$	$C_{16}H_{12}CdN_8S_2$
Temperature (K)	293(2)	293(2)	293(2)
FW	466.48	451.80	492.86
Wavelength (Å)	0.71073	0.71073	0.71073
Crystal system	Monoclinic	Monoclinic	Monoclinic
Space group	$C2/c$	$C2/c$	$P2(1)/c$
Unit cell dimensions, a (Å), b (Å), c (Å)	22.906(3), 6.730(2), 11.236(3)	27.106(4), 10.040(1), 7.442(1)	7.615(2), 10.017(3), 26.635(4)
α (deg.)	90	90	90
β (deg.)	111.711(8)	101.855(6)	94.229(5)
γ (deg.)	90	90	90
V (Å^3)	1609.2(6)	1982.1(4)	2026.0(9)
Z	4	4	4
D_{calc} (g cm^{-3})	1.925	1.514	1.616
$F(000)$	928	888	976
Absorption coefficient (mm^{-1})	2.915	1.321	1.302
Reflections collected/unique (R_{int})	7431/1470 (0.0190)	7285/2260 (0.0184)	27 657/3760 (0.0430)
Data/restraints/parameters	1470/0/114	1997/0/111	3760/12/244
R index ($I > 2\sigma(I)$)	$R_1 = 0.0346$, w$R_2 = 0.1310$	$R_1 = 0.0422$, w$R_2 = 0.1373$	$R_1 = 0.0454$, w$R_2 = 0.1238$
Goodness-of-fit on F^2	1.001	1.005	1.002
Largest difference in peak and hole (e Å^{-3})	0.679 and -0.578	1.273 and -0.759	0.645 and -1.123

[a] $R_1 = [\sum ||F_o| - |F_c||/\sum |F_o|]$, $wR_2 = \sum_W \left[\left| F_0^2 - F_c^2 \right|^2 \Big/ \sum_W \left(|F_W|^2 \right)^2 \right]^{1/2}$.

Table 2 Selected bond distances (Å) and angles (°) for complexes **1**, **2** and **3**[a]

Complexes 1

Cu(1)–N(1A)	1.926(3)	N(1A)–Cu(1)–S(1)	102.90(9)
Cu(1)–N(11)	2.008(3)	N(11)–Cu(1)–S(1B)	101.49(9)
Cu(1)–S(1)	2.458(1)	N(1A)–Cu(1)–N(11)	136.5(1)
Cu(1)–S(1B)	2.461(1)	S(1)–Cu(1)–S(1B)	106.98(3)
S(1)–C(1)	1.659(3)	C(1)–S(1)–Cu(1)	100.8(1)
N(1)–C(1)	1.147(4)	C(1)–N(1)–Cu(1C)	163.3(3)
Cu(1)–Cu(1B)	2.927(1)	N(1)–C(1)–S(1)	179.1(3)

Complexes 2

Cd(1)–N(1A)	2.308(2)	N(1A)–Cd(1)–N(1B)	180.0
Cd(1)–N(11)	2.368(2)	N(1A)–Cd(1)–N(11)	90.66(9)
Cd(1)–S(1)	2.7402(9)	N(11)–Cd(1)–S(1)	87.92(6)
S(1)–C(1)	1.644(3)	N(1A)–Cd(1)–S(1)	89.52(7)
N(1)–C(1)	1.146(4)	C(1)–S(1)–Cd(1)	99.4(1)
N(12)–C(16)	1.306(4)	N(1B)–Cd(1)–S(1)	90.48(7)
N(13)–C(16)	1.323(4)	N(1)–C(1)–S(1)	179.6(3)
N(12)–N(12E)	1.426(5)	C(1)–N(1)–Cd(1D)	166.1(3)

Complexes 3

Cd(1)–S(1)	2.770(2)	N(1A)–Cd(1)–N(2B)	174.9(2)
Cd(1)–S(2)	2.781(2)	N(1A)–Cd(1)–N(12C)	89.0(2)
Cd(1)–N(1A)	2.300(4)	N(1A)–Cd(1)–N(11)	91.0(2)
Cd(1)–N(2B)	2.312(4)	N(2B)–Cd(1)–N(11)	89.9(2)
Cd(1)–N(12C)	2.379(4)	S(1)–Cd(1)–S(2)	176.91(4)
Cd(1)–N(11)	2.396(4)	N(11)–Cd(1)–S(1)	90.6(1)
S(1)–C(1)	1.642(5)	N(1)–C(1)–S(1)	179.0(5)
S(2)–C(2)	1.634(5)	N(2)–C(2)–S(2)	178.1(5)
N(1)–C(1)	1.148(6)	C(1)–S(1)–Cd(1)	96.7(2)
N(2)–C(2)	1.149(6)	C(2)–S(2)–Cd(1)	103.2(2)

[a] Symmetry codes: for **1**, A: x, $-y + 2$, $z - 1/2$; B: $-x + 1/2$, $-y + 5/2$, $-z + 1$; C: x, $-y + 2$, $z + 1/2$; for **2**, A: x, $-y + 2$, $z + 1/2$; B: $-x + 1/2$, $y - 1/2$, $-z - 1/2$; C: $-x + 1/2$, $-y + 3/2$, $-z$; D: $-x + 1/2$, $y + 1/2$, $-z - 1/2$; E: $-x$, y, $-z + 1/2$; for **3**, A: $-x + 1$, $y + 1/2$, $-z + 1/2$; B: $-x$, $y - 1/2$, $-z + 1/2$; C: $x - 1$, $-y + 1/2$, $z - 1/2$.

In addition to the characteristic vibration bands of the aromatic heterocyclic at 1400–1625 cm^{-1}, near 1367 cm^{-1} (s), around 1420 cm^{-1}, strong adsorption bands of SCN$^-$ ligands appear at about 2120, 2104, 2104 cm^{-1} for **1**, **2** and **3** respectively. Furthermore, for bulk samples of **1**, **2** and **3**, the phase purity is confirmed by comparing their PXRD data with the simulated data from their CIF files, as shown in ESI (Fig. S7–S9, ESI†).

Structure of $[Cu_2(4,4'\text{-Hbpt})(SCN)_2]_n$ (1)

The structure of **1** exhibits a 3-D framework with primitive cubic (pcu) topology in which there is only one unique Cu(I) ion in the asymmetric unit (Fig. 1). The Cu(I) cation is in a tetrahedral environment consisting of two S atoms from two distinct $\mu_{1,1,3}$-SCN$^-$ groups, one N atom from a $\mu_{1,1,3}$-SCN$^-$ group, and one $N_{pyridyl}$ atom from a 4,4′-Hbpt ligand. The bond angles around the Cu1 center range from 101.49(9)–136.5(1)°, the average Cu–S length is 2.460(1) Å, the distance of Cu1–N11 is 2.008(3) Å, while the length of Cu1–N1A is 1.926(3) Å (Fig. 1a). Interestingly, adjacent two Cu(I) atoms are bridged by two S atoms from two $\mu_{1,1,3}$-SCN$^-$ groups to form a dinuclear $[Cu_2SCN_2]$ secondary building unit (SBU). The Cu···Cu separation in the SBU is 2.927(1) Å, which is little longer than the sum of van der Waals radii for copper (2.8 Å),[12] suggesting weak copper–copper interactions. These SBUs are further linked by another two $\mu_{1,1,3}$-SCN$^-$ groups to form a wave-like neutral $[Cu_2(SCN)_2]_n$ layer with (4.8^2) topology consisting of 4-membered $[Cu_2S_2]$ rings and 8-membered $[Cu_4(SCN)_4]$ macrocycles (Fig. 1b). If the dinuclear $[Cu_2]$ subunits are simplified as 4-connected nodes, the wave-like layer present a simple (4, 4) topology. These wave-like layers are further linked by 4,4′-Hbpt ligands along the a-axis to form a 3-D structure (Fig. 1c and d). If the Cu(I) cations
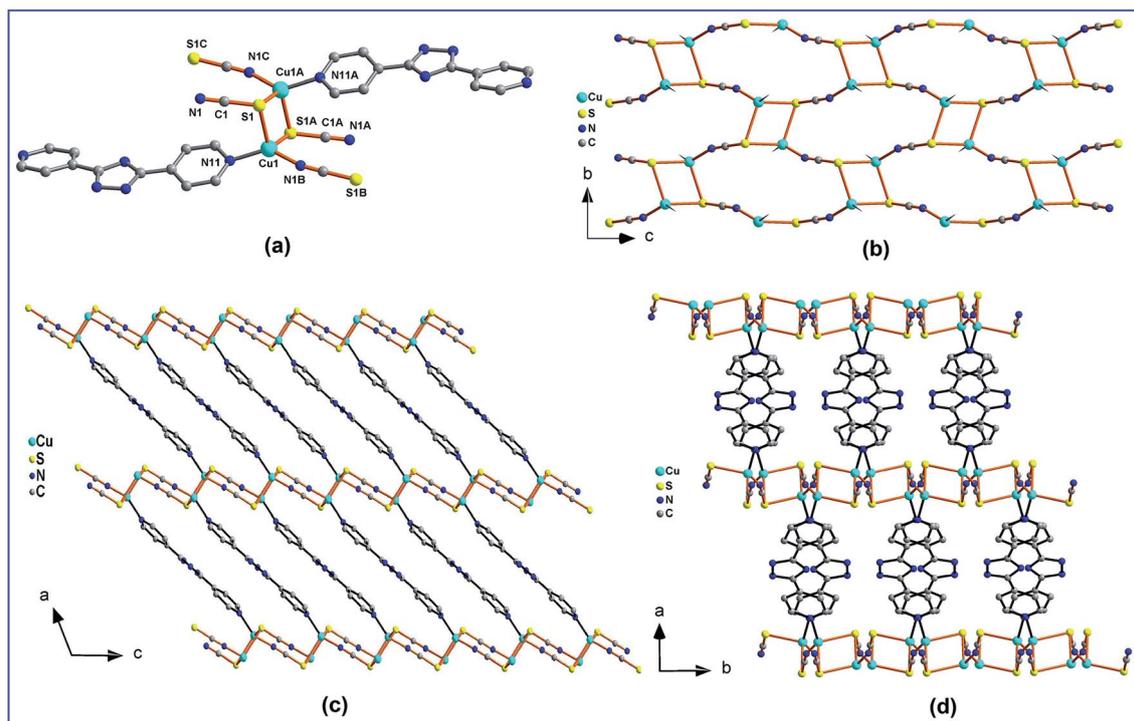
Fig. 1 (a) View of the coordination environment of copper(I) cations in **1**, symmetry codes: *A* −*x* + 1/2, −*y* + 5/2, −*z* + 1; *B x*, −*y* + 2, *z* − 1/2; *C* −*x* + 1/2, *y* + 1/2, −*z* + 3/2. (b) 2-D 4.8² topological layer consisting of μ₃-SCN⁻ anions and Cu(I) cations, the wedge-like lines represent the 4,4′-Hbpt ligands; (c) view of the 3D network of **1** along the *b*-axis; (d) view of the 3D network of **1** along the *c*-axis. All H atoms are omitted for clarity.

are considered as 4-connected nodes, μ₃-SCN⁻ groups are taken as 3-connected nodes, while the 4,4′-Hbpt ligands are regarded as bridging linkers, the framework has the total point symbol of $\{4\cdot6\cdot8\}\{4\cdot6^2\cdot8^3\}$ as analyzed by the TOPOS 4.0 program.[13] This topology can be evolved as the known uninodal α-Po primitive cubic (pcu) topology (Fig. S1, ESI†) with the point symbol of $\{4^{12}\cdot6^3\}$, when the [Cu₂] subunit are regarded as 6-connected nodes, while SCN⁻ groups and 4,4′-Hbpt ligands are considered as bridging linkers.

Structure of $[Cd(4,4′\text{-Hbpt})(SCN)_2]_n$ (2)

The structure of **2** features a 3-D 6-connected framework with α-Po pcu topology. As shown in Fig. 2a, there are one cadmium(II) cation, two 4,4′-Hbpt ligands and four thiocyanate anions in the repeating unit. The Cd1 cation locates in an elongated octahedral coordination geometry which consists of two N atoms and two S atoms from four distinct μ-SCN groups, as well as two N_pyridyl atoms from two distinct 4,4′-Hbpt ligands. The bond length of Cd–N_SCN is 2.308(2) Å, Cd–N_pyridyl is 2.368(2) Å, which are shorter than the bond distance of Cd–S_SCN (2.7402(9) Å). Unlike the SCN⁻ groups in **1**, all the SCN⁻ groups in **2** adopt μ₁,₃-bridging mode and link Cd(II) ions to form a 2-D fluctuant $[Cd(\mu\text{-SCN})_2]_n$ layer containing 8-membered $[Cd_4(\mu\text{-SCN})_4]$ macrocycles (Fig. 2b). These neutral layers display (4, 4) topological nets when Cd(II) cations are regarded as 4-connected nodes while SCN⁻ groups are considered as bridging linkers. These fluctuant $[Cd(\mu\text{-SCN})]_n$ layers are further connected by bridging 4,4′-Hbpt ligands to form 3-D framework with α-Po pcu

topology (Fig. S2, ESI†), when the 4,4′-Hbpt ligands are also taken as bridging linkers. It should be noted, the framework has two kinds of channels, one kind display rhombic channels with the effective size of *ca.* 6.5 × 10.9 Å² along the *c*-axis (Fig. 2c), while the other kind represent rectangular channels with the effective size of *ca.* 1.9 × 12.2 Å² along the *b*-axis (Fig. 2d). There is no solvent molecules reside these channels, although the crystal has about 24.4% void space according to the PLATON program.[14]

Structure of $[Cd(4,4′\text{-Hbpt})(SCN)_2\cdot CH_3CN]_n$ (3)

Similar to the structure of **2**, complex **3** also features a 3-D 6-connected framework with α-Po pcu topology, and also are constructed by 4,4′-Hbpt ligands connecting fluctuant $[Cd(\mu\text{-SCN})_2]_n$ layers. However, the two complexes crystallize in different space groups, and the 4,4′-Hbpt ligands and $[Cd(\mu\text{-SCN})_2]_n$ layers in them have different spatial orientations. As shown in Fig. 3a, there are one cadmium(II) cation, two 4,4′-Hbpt ligands and four thiocyanate anions in the repeating unit. The Cd1 cation locates in an elongated octahedral coordination geometry which consists of two N atoms and two S atoms from four symmetry-related μ-SCN⁻ groups, as well as two N_pyridyl atoms from two symmetry-related 4,4′-Hbpt ligands. The average bond length of Cd–N_SCN is 2.306(4) Å, Cd–N_pyridyl is 2.388(4) Å, which are shorter than the average bond distance of Cd–S_SCN (2.776(2) Å). Similar to the SCN⁻ groups in **2**, all the SCN⁻ groups in **3** adopt μ₁,₃-bridging mode and link Cd(II) ions to form a 2-D fluctuant $[Cd(\mu\text{-SCN})_2]_n$ layer containing
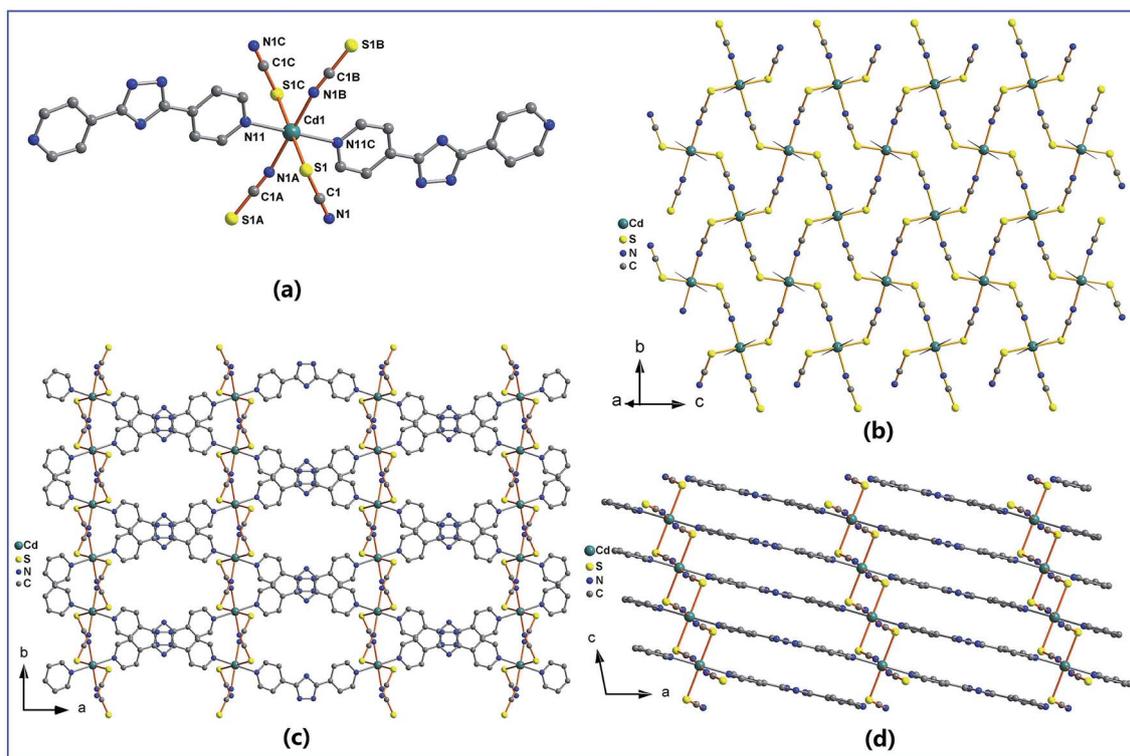
Fig. 2 (a) View of the coordination environment of cadmium cations in **2**, symmetry codes: A *x*, −*y* + 2, *z* + 1/2, B −*x* + 1/2, *y* − 1/2, −*z* − 1/2, C −*x* + 1/2, −*y* + 3/2, −*z*; (b) 2-D (4, 4) layer consisting of μ$_2$-SCN$^−$ anions and Cd(ɪɪ) cations, the wedge-like lines represent the 4,4′-Hbpt ligands; (c) view of the 3D network of **2** along the *c*-axis; (d) view of the 3D network of **2** along the *b*-axis. All H atoms are omitted for clarity.

8-membered [Cd$_4$(μ-SCN)$_4$] macrocycles (Fig. 3b). These neutral layers display (4, 4) topological nets when Cd(ɪɪ) cations are regarded as 4-connected nodes while SCN$^−$ groups are considered as bridging linkers. These fluctuant [Cd(μ-SCN)]$_n$ layers are further connected by bridging 4,4′-Hbpt ligands to form 3-D framework with α-Po pcu topology (Fig. S3, ESI†), when the 4,4′-Hbpt ligands are also taken as bridging linkers. It should be noted, the framework has two kinds of channels, one kind display hexagonal channels with the effective size of *ca.* 6.9 × 10.4 Å^2 along the *a*-axis (Fig. 3c), while the other kind represent rectangular channels with the effective size of *ca.* 2.0 × 12.3 Å^2 along the *b*-axis (Fig. 3d). The CH$_3$CN solvent molecules are located in the channels along the *a*-axis while the channels along the *b*-axis are almost vacant.

Photoluminescent properties

Upon photo-excitation at 380 nm, complex **1** exhibits a strong and sharp red emission band with CIE coordinates (0.549, 0.322) in the solid-state at 727 nm, complex **2** displays a strong blue emission band in the solid-state at 452 nm with CIE coordinates (0.262, 0.265), complex **3** shows a strong blue emission band in the solid-state at 446 nm with CIE coordinates (0.171, 0.148), while the 4,4′-Hbpt ligand presents a relatively weak blue emission band in the solid-state at 450 nm (Fig. 4). Comparing with the emission peak of 4,4′-Hbpt ligand, the emission peak of **1** exhibits a large red shift of 277 nm and a very different band shape, indicating the 4,4′-Hbpt ligand and **1**

possess different photoluminescent mechanism. While for **2** and **3**, both the locations and the shapes of the emission are very similar to those of the 4,4′-Hbpt ligand, suggesting the 4,4′-Hbpt ligand, **2** and **3** probably have similar photoluminescent process.

Density functional theory (DFT) calculation of the electronic band structures of the present three complexes along with density of states (DOS) was carried out with the CASTEP code (Fig. S4, S5 and S6 and their explanations, ESI†), which uses one of the three nonlocal gradient corrected exchange-correlation functionals (GGA-PBE). As shown in Fig. 5, for complexes **1**, the top of valence bands (VBs) are mostly formed by the hybridizations of Cu-3d state (29.2 electrons per eV), SCN$^−$-2p states (12.1 electrons per eV) and 4,4′-Hbpt-2p states (17.3 electrons per eV), in which Cu-3d state peak locates around −1.3 eV, SCN$^−$-2p states peak settle around −2.7 eV, and 4,4′-Hbpt-2p states lies around −2.9 eV. The bottom of conduction bands (CBs) are mainly contributed from the 4,4′-Hbpt-2p states (10.7 electrons per eV). Accordingly, the origin of the emission band of **1** may be mainly ascribe to the coupling of metal-to-ligand charge transfer (MLCT) and ligand-to-ligand charge transfer (LLCT). For MLCT, the electrons are transferred from the copper (Cu-3d state, VBs) to the unoccupied π* orbitals of 4,4′-Hbpt ligands (4,4′-Hbpt-2p states, CBs), while for LLCT, the electrons are transferred from the occupied π orbitals of SCN$^−$ groups and 4,4′-Hbpt ligands (SCN$^−$-2p and 4,4′-Hbpt-2p states, VBs) to the unoccupied π* orbitals of 4,4′-Hbpt ligands (4,4′-Hbpt-2p states, CBs).
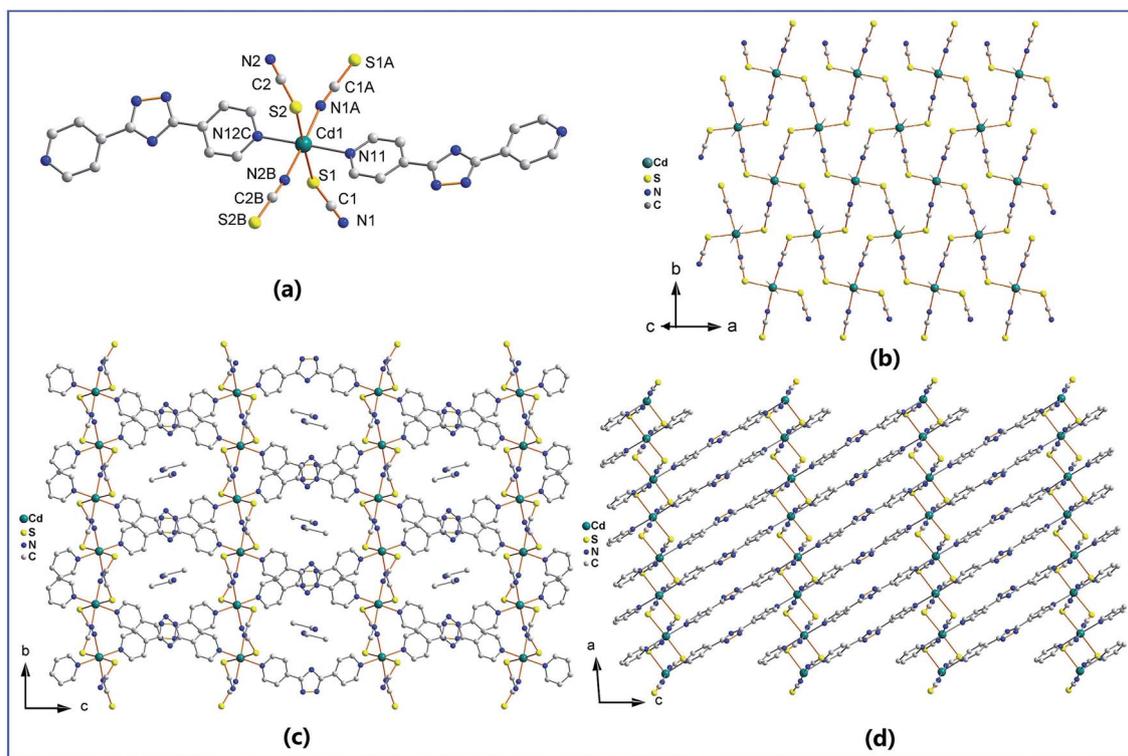
Fig. 3 (a) View of the coordination environment of cadmium cations in **3**, symmetry code: *A* −*x* + 1, *y* + 1/2, −*z* + 1/2, *B* −*x*, *y* + 1/2, −*z* + 1/2, *C x* − 1, −*y* + 1/2, *z* − 1/2; (b) 2-D (4, 4) layer consisting of μ₂-SCN⁻ anions and Cd(ɪɪ) cations, the wedge-like lines represent the 4,4′-Hbpt ligands; (c) view of the 3D network of **3** along the *a*-axis, and the CH₃CN solvents resides the channels along the *a*-axis; (d) view of the 3D network of **3** along the *b*-axis. All H atoms are omitted for clarity.
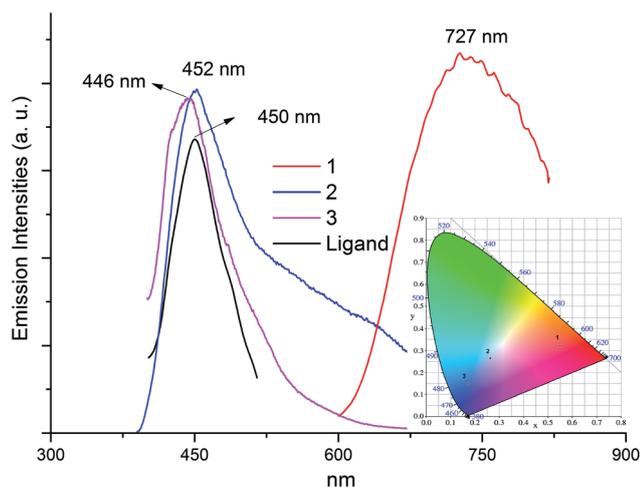
Fig. 4 Solid-state electronic emission spectra and CIE chromaticity diagram (inset) of **1**, **2**, **3** and 4,4′-Hbpt ligand upon photo-excitation at 380 nm at room temperature.

Fig. 5 The total and partial density of states of **1**. The Fermi level is set at 0 eV.

For complex **2** (Fig. 6), the top of VBs are mostly formed by the mixture of SCN⁻-2p states (20.3 electrons per eV) and 4,4′-Hbpt-2p states (20.2 electrons per eV), in which SCN⁻-2p states peak locates around −0.2 eV and 4,4′-Hbpt-2p states peak settle around −1.7 eV. The bottom of CBs are mainly contributed from 4,4′-Hbpt-2p states (13.8 electro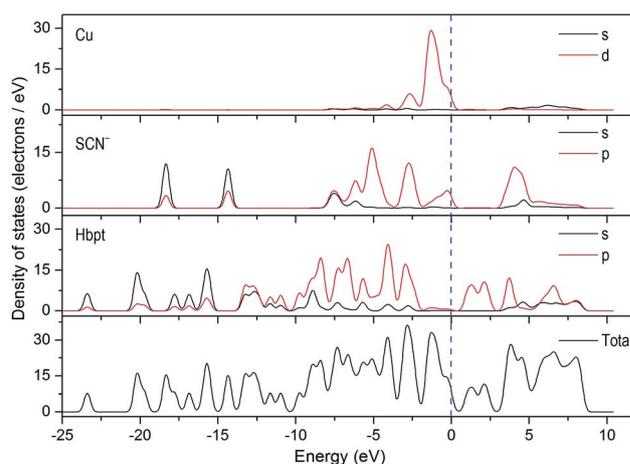ns per eV). Accordingly, the origin of the emission band of **2** may be mainly ascribe to ligand-to-ligand charge transfer (LLCT) where the electrons are transferred from the occupied π orbitals of SCN⁻ groups and 4,4′-Hbpt ligands (SCN⁻-2p and 4,4′-Hbpt-2p states, VBs) to the unoccupied π* orbitals of 4,4′-Hbpt ligands (4,4′-Hbpt-2p states, CBs).

For complex **3** (Fig. 7), the top of VBs are mostly formed by the hybridizations of SCN⁻-2p states (41.7 electrons per eV) and
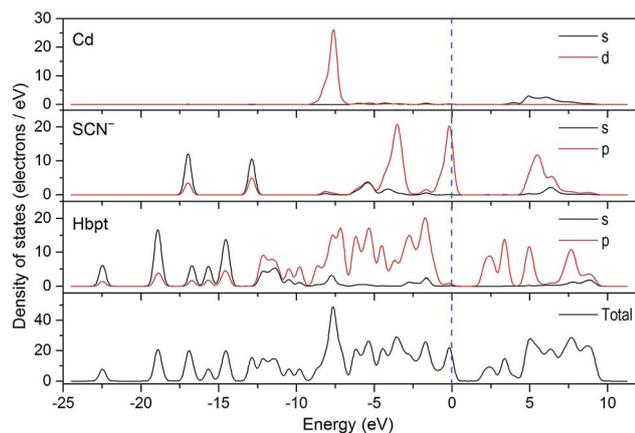
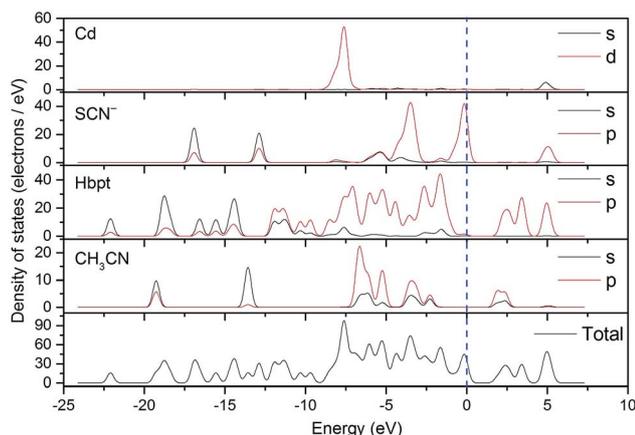Fig. 6 The total and partial density of states of **2**. The Fermi level is set at 0 eV.

Fig. 7 The total and partial density of states of **3**. The Fermi level is set at 0 eV.

4,4′-Hbpt-2p states (44.2 electrons per eV), in which SCN^--2p states peak locates around -0.2 eV and 4,4′-Hbpt-2p states peak settle around -1.6 eV. The bottom of CBs are mainly contributed from the 4,4′-Hbpt-2p states (18.9 electrons per eV), mixing with small CH_3CN-2p states (6.2 electrons per eV). Accordingly, the origin of the emission band of **3** may be mainly ascribe to ligand-to-ligand charge transfer (LLCT) where the electrons are transferred from the occupied π orbitals of SCN^- groups and 4,4′-Hbpt ligands (SCN^--2p and 4,4′-Hbpt-2p states, VBs) to the unoccupied π* orbitals of 4,4′-Hbpt ligands and CH_3CN guest molecules (4,4′-Hbpt-2p and CH_3CN-2p states, CBs).

It should be noted, complex **1** and complexes **2** and **3** exhibit very different emission mechanism although they have similar structure constructed by 4,4′-Hbpt ligands connecting neutral d^{10} metal thiocyanate layer. The main reason may be ascribed to their different components of the top of VBs since Cd-4d states has much lower energy level than Cu-3d states. Considering the extended π-electron conjugated system of 4,4′-Hbpt ligands, the origin of the emission band of pure 4,4′-Hbpt ligands may

probably be ascribe to intraligand charge transfer (ILCT) where the electrons are transferred from their occupied π orbitals to their unoccupied π* orbitals. Meanwhile, as shown in Fig. 6 and 7, the energy level spacing between π orbitals of SCN^- and π* orbitals of 4,4′-Hbpt, π orbitals of 4,4′-Hbpt and π* orbitals of 4,4′-Hbpt, π orbitals of 4,4′-Hbpt and π* orbitals of CH_3CN are comparable, therefore complex **2**, **3** and pure ligand exhibit similar emission peak.

Thermal stability

Complexes **1**, **2** and **3** are stable in air, and can maintain their crystallinity at room temperature for several days. The TGA curves show that compounds **1**, **2** decompose at the decomposition point T_{onset} of about 256, 241 °C (Fig. S10 and S11, ESI†), respectively, indicating they are stable materials for practical application. While for compound **3**, it decomposes in three steps with the first weight change of about 8.1% (Fig. S12, ESI†), which roughly corresponds to the losing of one CH_3CN guest molecule (calc. 8.33%). And the second stage of decomposition starts at about 240 °C. The further detailed decomposition mechanisms of the three complexes are too complex to explain at present. Together with the efficient luminescent properties, the present three complexes are good candidates as luminescent materials.

Conclusions

In summary, three pillared-layered IOHPs constructed by 4,4′-Hbpt ligands connecting neutral wave-like d^{10} metal thiocyanate layers were synthesized, and the relationships between their structures and photoluminescence were well explored *via* DFT analysis. The synthesis strategy of the three complexes may be spread to prepare the family of pillared-layered IOHPs constructed by conjugated organic ligands bridging neutral layered d^{10} metal halides/pseudohalides. In the three IOHPs, conjugated 4,4′-Hbpt ligands play important roles in the emission process of IOHPs, and may largely tune the structures and luminescence properties of d^{10} metal thiocyanate. Further experiments based on this family of pillared-layered IOHPs are undergoing. Investigations of the luminescence behaviors of these IOHPs will be helpful for the design and synthesis of more efficient luminescent materials.

Conflicts of interest

There are no conflicts to declare.

Acknowledgements

Notes and references

1 For latest reviews, see: (*a*) M. M. Unterlass, *Eur. J. Inorg. Chem.*, 2016, 1135–1156; (*b*) S. Taleghani, M. Mirzaei, H. Eshtiagh-Hosseini and A. Fronterab, *Coord. Chem. Rev.*, 2016, **309**, 84–106; (*c*) E. Cariati, E. Lucentib, C. Bottad, U. Giovanellad, D. Marinottoc and S. Righettoa, *Coord. Chem. Rev.*, 2016, **306**, 566–614; (*d*) M. Mirzaeia, H. Eshtiagh-Hosseinia, M. Alipoura and A. Fronterab, *Coord. Chem. Rev.*, 2014, **275**, 1–18; (*e*) U. Schubert, *Chem. Soc. Rev.*, 2011, **40**, 575–582; (*f*) J. C. Tan and A. K. Cheetham, *Chem. Soc. Rev.*, 2011, **40**, 1059–1080.

2 (*a*) S. Suckert, M. Rams, M. Böhme, L. S. Germann, R. E. Dinnebier, W. Plass, J. Wernera and C. Näther, *Dalton Trans.*, 2016, **45**, 18190–18201; (*b*) J. Werner, Z. Tomkowicz, T. Reinert and C. Näther, *Eur. J. Inorg. Chem.*, 2015, 3066–3075; (*c*) E. Shurdha, S. H. Lapidus, P. W. Stephens, C. E. Moore, A. L. Rheingold and J. S. Miller, *Inorg. Chem.*, 2012, **51**, 9655–9665; (*d*) M. Wriedt and C. Näther, *Z. Anorg. Allg. Chem.*, 2010, **636**, 569–575; (*e*) M. Wriedt, S. Sellmer and C. Näther, *Inorg. Chem.*, 2009, **48**, 6896–6903; (*f*) A. D. Jana, S. C. Manna, G. M. Rosair, M. G. B. Drew, G. Mostafa and N. R. Chaudhuri, *Cryst. Growth Des.*, 2007, 7(7), 1365–1372; (*g*) G. D. Munno, D. Armentano, T. Poerio, M. Julve and J. A. Real, *J. Chem. Soc., Dalton Trans.*, 1999, 1813–1817.

3 (*a*) Y. Bai, J.-L. Wang, D.-B. Dang, M.-M. Li and J.-Y. Niu, *CrystEngComm*, 2012, **14**, 1575–1581; (*b*) I. Jeß, J. Boeckmann and C. Näther, *Dalton Trans.*, 2012, **41**, 228–236; (*c*) J. Boeckmann, T. Reinert, I. Jeß and C. Näther, *Z. Anorg. Allg. Chem.*, 2011, **637**, 1137–1144; (*d*) G. Bhosekar, J. Boeckmann, I. Jeß and C. Näther, *Z. Anorg. Allg. Chem.*, 2010, **636**, 2595–2601; (*e*) G. Yang, H.-G. Zhu, B.-H. Liang and X.-M. Chen, *J. Chem. Soc., Dalton Trans.*, 2001, 580–585; (*f*) A. J. Blake, N. R. Brooks, N. R. Champness, M. Crew, L. R. Hanton, P. Hubberstey, S. Parsons and M. Schröder, *J. Chem. Soc., Dalton Trans.*, 1999, 2813–2817.

4 (*a*) L. Li, C.-H. Wang, X.-L. Zhang and X. Liu, *Eur. J. Inorg. Chem.*, 2015, 859–863; (*b*) X. Liu, L. Li, Y.-Z. Yang and K.-L. Huang, *Dalton Trans.*, 2014, **43**, 4086–4092; (*c*) X. Liu, Y.-Z. Yang, C.-H. Wang and K.-L. Huang, *Aust. J. Chem.*, 2013, **66**, 989–992; (*d*) X. Liu and K.-L. Huang, *Inorg. Chem.*, 2009, **48**, 8653–8655; (*e*) X. Liu, K.-L. Huang, G.-M. Liang, M.-S. Wang and G.-C. Guo, *CrystEngComm*, 2009, **11**, 1615–1620; (*f*) X. Liu and G.-C. Guo, *Cryst. Growth Des.*, 2008, **8**, 776–778; (*g*) X. Liu, G.-C. Guo, M.-L. Fu, W.-T. Chen, M.-S. Wang and J.-S. Huang, *Inorg. Chem.*, 2006, **45**, 3679–3685; (*h*) X. Liu, G.-C. Guo, M.-L. Fu, W.-T. Chen, J.-Z. Zhang and J.-S. Huang, *Dalton Trans.*, 2006, 884–886; (*i*) X. Liu, G.-C. Guo, A.-Q. Wu, L.-Z. Cai and J.-S. Huang, *Inorg. Chem.*, 2005, **44**, 4282–4286; (*j*) X. Liu and G.-C. Guo, *Aust. J. Chem.*, 2008, **61**, 481–483; (*k*) X. Liu, G.-C. Guo, M.-L. Fu, J.-P. Zou, F.-Q. Zheng and J.-S. Huang, *Inorg. Chim. Acta*, 2006, **359**, 1643–1649.

5 (*a*) V. W.-W. Yam and K. K.-W. Lo, *Chem. Soc. Rev.*, 1999, **28**, 323–334; (*b*) P. Ford and A. Vogler, *Acc. Chem. Res.*, 1993, **26**, 220–226.

6 H. Zhang, X. Wang, K. Zhang and B. K. Teo, *Coord. Chem. Rev.*, 1999, **183**, 157–195.

7 (*a*) C.-H. Wang, X. Liu, Y.-Z. Yang and K.-L. Huang, *Inorg. Chim. Acta*, 2013, **407**, 116–120; (*b*) F.-P. Huang, Q. Zhang, Q. Yu, H.-D. Bian, H. Liang, S.-P. Yan, D.-Z. Liao and P. Cheng, *Cryst. Growth Des.*, 2012, **12**, 1890–1898; (*c*) F.-P. Huang, J.-L. Tian, W. Gu, X. Liu, S.-P. Yan, D.-Z. Liao and P. Cheng, *Cryst. Growth Des.*, 2010, **10**, 1145–1154; (*d*) F.-P. Huang, J.-L. Tian, G.-J. Chen, D.-D. Li, W. Gu, X. Liu, S.-P. Yan, D.-Z. Liao and P. Cheng, *CrystEngComm*, 2010, **12**, 1269–1279; J.-P. Zhang, Y.-Y. Lin, X.-C. Huang and X.-M. Chen, *Cryst. Growth Des.*, 2006, **6**, 519–523.

8 (*a*) J. E. Endicott, Y. J. Chen and P. H. Xie, *Coord. Chem. Rev.*, 2005, **249**, 343–373; (*b*) O. Maury, L. Viau, K. Senechal, B. Corre, J. P. Guegan, T. Renouard, I. Ledoux, J. Zyss and H. Le Bozec, *Chem.–Eur. J.*, 2004, **10**, 4454–4466.

9 C.-H. Wang, X. Liu, Y.-Z. Yang and K.-L. Huang, *Inorg. Chim. Acta*, 2013, **407**, 116–120.

10 *CrystalClear, Version 1.35, Software User's Guide for the Rigaku R Axis, and Mercury and Jupiter CCD Automated X-ray Imaging System*, Rigaku Molecular Structure Corporation, Utah, 2002.

11 *SHELXTL, Version 5, Reference Manual*, Siemens Energy & Automation Inc., Madison, WI, 1994.

12 J. C. Slater, *J. Chem. Phys.*, 1964, **41**, 3199–3204.

13 V. A. Blatov, *Struct. Chem.*, 2012, **23**, 955–963.

14 A. L. Spek, *J. Appl. Crystallogr.*, 2003, **36**, 7–13.